MD-Vol. 68
AMD-Vol. 215

# MECHANICS OF PLASTICS AND PLASTIC COMPOSITES – 1995 –

**presented at**
THE 1995 ASME INTERNATIONAL
MECHANICAL ENGINEERING CONGRESS AND EXPOSITION
NOVEMBER 12–17, 1995
SAN FRANCISCO, CALIFORNIA

**sponsored by**
THE MATERIALS DIVISION, ASME
THE APPLIED MECHANICS DIVISION, ASME

**edited by**
MARY C. BOYCE
MASSACHUSETTS INSTITUTE OF TECHNOLOGY

THE AMERICAN SOCIETY OF MECHANICAL ENGINEERS
UNITED ENGINEERING CENTER / 345 EAST 47TH STREET / NEW YORK, N.Y. 10017

MD-Vol. 68/AMD-Vol. 215, Mechanics of Plastics and
Plastic Composites
ASME 1995

# A Phenomenological Constitutive Model for Rigid Polymeric Foam[#]

**Michael A. Puso**
Applied Mechanics Group, DTED
Lawrence Livermore National Laboratory
Livermore, California 94550

**Sanjay Govindjee**
Department of Civil Engineering
University of California at Berkeley
Berkeley, California 94720

## ABSTRACT

An orthotropic rate independent plasticity and viscoplasticity constitutive law for rigid low density polymeric foams is presented. A multi-surface yield criterion is used in the constitutive model to represent the envelope of failure surfaces given by Gibson et. al. (1989) for cellular materials. An inelastic flow direction is selected to simulate the near zero "plastic Poisson's ratio" observed in many experimental tests. A special orthotropic hardening law is also developed that captures the extreme stiffening due to densification at very large strains. Details involving loading and unloading conditions and discrete algorithms for numerical implementation are discussed. The rate dependencies are modeled by a power law viscoplasticity relation. The model is implemented in the finite element code DYNA3D and is used to simulate experimental results.

## 1. INTRODUCTION

Low density rigid polymeric foams are an effective means of absorbing energy from impact and have many engineering applications such as automobile crash padding and packaging. This class of foams are typically composed of polyurethane (rigid), polystyrene or polymethacrylimid and are closed cell and range in relative density ($\rho_{rel} = \rho_{foam}/\rho_{solid}$) from 0.02 to 0.4. The energy absorbing capacity of this material derives from its ability to undergo large deformations while maintaining a near constant stress value with little rebound; see e.g. Fig. 1 which shows the response of a 3 pcf (lbf per cubic foot) foam in uniaxial compression. The elastic behavior of these foams has been characterized by Gibson and Ashby (1988) and the failure (or yield criterion) has been characterized by Gibson et. al. (1989) and Triantafillou et. al. (1989). In the present work, a phenomenological orthotropic rate independent plasticity and viscoplasticity formulation are developed using the failure

[#] This work was performed under the auspices of DOE Contract W-ENG-4393-30 with the University of California.

envelope given by Gibson et. al. (1989). In order to extend the work of Gibson, it was necessary to provide a flow law, a hardening law and an evolution equation for the rate dependency.

In what follows, a yield surface is proposed to be formed from the non-smooth intersection of several surfaces in stress space. This is coupled to a non-associative flow law which precludes the use of a "closest point projection algorithm" (Simo et. al., 1988) as is typically used in multisurface plasticity. Thus, a specially developed return mapping algorithm for this model is presented below. The hardening law for the model is based on an effective stress notion which was numerically expedient and seen to be successful in fitting experimental results. A power law version of the model is also presented below; it is based on the Duvaut-Lions (1972) viscoplasticity formulation. In the remainder of the paper: the constitutive law is developed in Sections 2 and 3; model verification using the explicit finite element code DYNA3D (Whirley and Englemann, 1993) is shown in Section 4.

## 2. MECHANICAL BEHAVIOR OF FOAM

Three of the basic regions of foam deformation: elastic, plateau and densification are illustrated by the uniaxial compression curve shown in Fig. 1. In the small strain elastic region, the deformation is mainly due to bending and axial stretching of cell walls (Gibson and Ashby, 1988). At some point the cell walls and struts begin to yield due to the plastic nature of the rigid polymers from which the foams are made. When this occurs the stress begins to plateau as seen in Fig. 1. As the deformation progresses, gas is expelled due to popping of the cell walls and cells walls begin to contact and the materials stiffens as seen in the densification region.

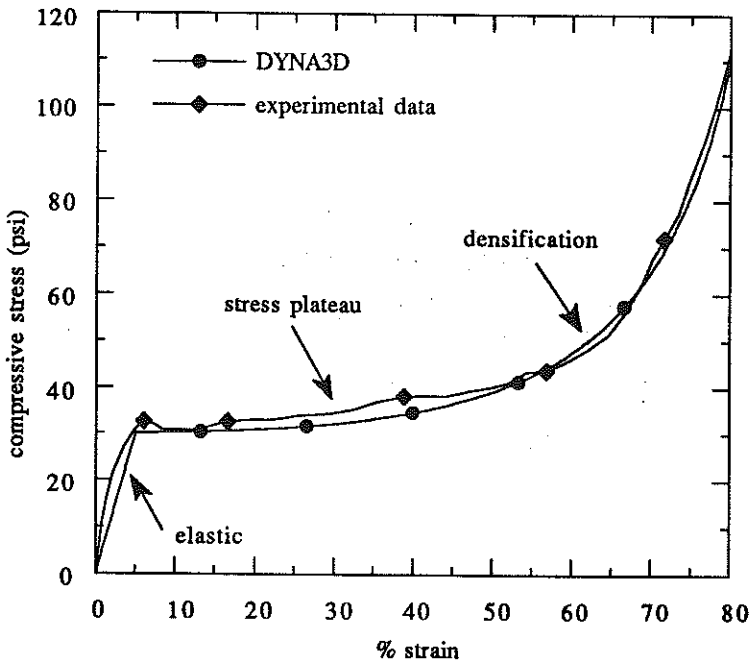


Fig. 1. Three regions of stress seen from the uniaxial compression test (Rossi et. al., 1992) of a 3 pcf polyurethane foam along with DYNA3D simulation.

The multiaxial behavior of foam is more complex. Additionally, the foams are often quite anisotropic due to preferred cell growth in the foam rise direction during manufacture/forming. A mechanistic development of the failure surfaces for foam under multiaxial loads was given by Gibson et. al. (1989). Often during forming, surface tension draws the polymer toward cell wall edges causing

the cell walls to become thin and the edges to become strut like. Assuming strut like behavior of the cell walls, Gibson used a dimensional analysis argument to calculate the bending moments and axial forces in the struts of a given unit cell under multiaxial loading conditions. Assuming three different "failure" mechanisms, Gibson derived the failure surfaces in stress space by calculating the bending moments and axial forces necessary to fail the struts. The three failure mechanisms: plastic hinges, elastic buckling, and tensile cracking are shown schematically in Fig. 2. These failure surfaces are shown for triaxial loading conditions in Fig.3.

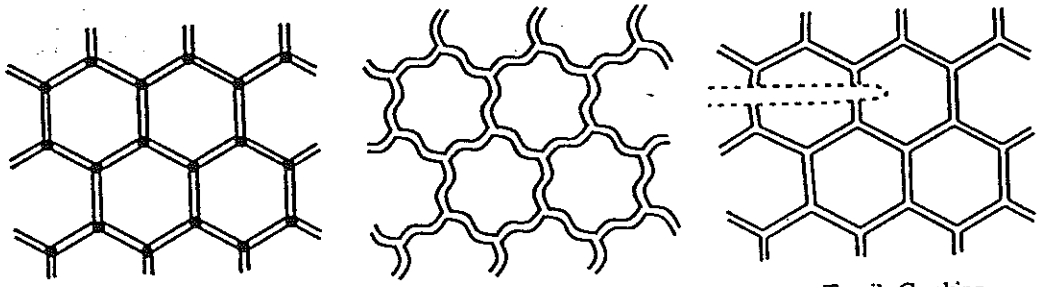


Fig. 2. The three failure mechanism seen in rigid polymeric foams.

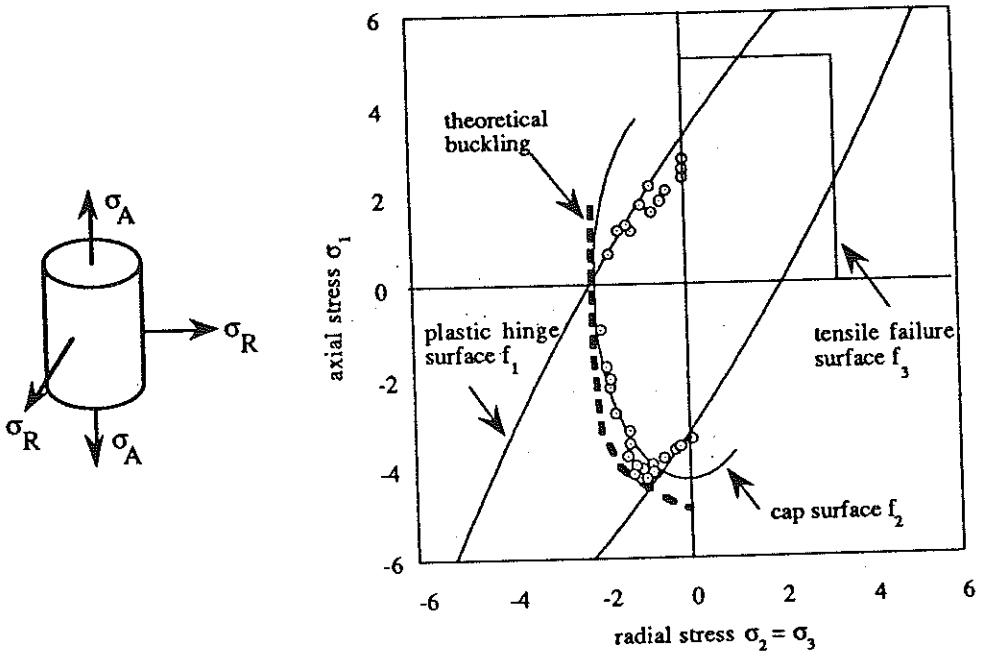


(a) (b)

Fig. 3. (a) Triaxial loading conditions where $\sigma_A = \sigma_1$ and $\sigma_R = \sigma_2 = \sigma_3$. (b) Experimental data (Triantafillou et. al., 1989) for compressive radial stress at failure in triaxial tests along with the envelope of failure surfaces $f_1$, $f_2$, $f_3$.

The plastic hinge surface $f_1(\sigma)$ (Eq. 1) was formulated by summing the stresses from bending and axial loads and setting them equal to the value necessary to produce a fully developed plastic hinge in the struts.

$$f_1(\sigma) = \sqrt{\tilde{J}} + a\,\tilde{I}^2 - 1 = 0 \tag{1}$$

where ,

$$\tilde{J}(\sigma) = \frac{1}{2}\left[\left(\frac{\sigma_{11}}{k_{11}} - \frac{\sigma_{22}}{k_{22}}\right)^2 + \left(\frac{\sigma_{22}}{k_{22}} - \frac{\sigma_{33}}{k_{33}}\right)^2 + \left(\frac{\sigma_{33}}{k_{33}} - \frac{\sigma_{11}}{k_{11}}\right)^2\right] + 3\left[\left(\frac{\sigma_{12}}{k_{12}}\right)^2 + \left(\frac{\sigma_{23}}{k_{23}}\right)^2 + \left(\frac{\sigma_{31}}{k_{31}}\right)^2\right] \tag{2}$$

$$\tilde{I}(\sigma) = \frac{\sigma_{11}}{k_{11}} + \frac{\sigma_{22}}{k_{22}} + \frac{\sigma_{33}}{k_{33}} \tag{3}$$

$k_{ij} > 0$ are the orthotropic yield parameters, $a = 0.09\ \rho_{rel}$ and $\rho_{rel}$ is the relative density[1].

The buckling surface was calculated by assuming buckling modes for a representative tetrahedron of cellular struts which comprise the foam. A closed form relation such as (1) is not available for multiaxial loading. For the purposes of this work the following curve fit of the theoretical buckling surface in triaxial space is proposed to represent the buckling surface. Eq. (4) shows the "cap" used to fit the buckling surface:

$$f_2(\sigma) = \tilde{J} + \frac{1}{R^2}\left(\tilde{I}^2 - h^2\right) = 0 \tag{4}$$

where R and h are determined from experiment.

The tensile failure represents the brittle fracture due to the propagation of cracks in the foam. The failure surface is formed by the maximum principle tensile stress $\sigma_i$ and is given by:

$$f_3(\sigma) = \max(\sigma_i) - K^*_{IC}/\sqrt{\pi c} = 0 \tag{5}$$

where $K^*_{IC}$ is the fracture toughness and 2c is the length of the longest crack. $f_3(\sigma)$ would be calibrated from a uniaxial tension test. In what follows, $f_3(\sigma)$ is ignored since such materials are predominately used in compression applications. In a more complete model this would be used as a damage surface.

The hardening exhibited at large volumetric compression is caused by increased contact of cell walls and struts as the free volume diminishes. Although closed cell foams have entrapped air that would experience increased hydrostatic compression, it is seen for the class of rigid foams that cell walls rupture once yield has occurred and most of the air escapes (Patel and Finnie, 1969). It is assumed that the total stress supported by the foam after yielding is due to contributions of the elastic axial and bending stresses in the cellular matrix and contact of adjacent cell walls and struts as they sandwich together. This provides the following effective stress formulation:

$$\sigma = \sigma^c + \sigma^d \tag{6}$$

where $\sigma^c$ is the stress due to bending and axial loads in the struts and $\sigma^d$ is the stress due to densification. Since the failure mechanisms are caused by cell wall bending and axial forces, the stress used for the failure surfaces and invariants in (1) - (5) are replaced by $\sigma^c$, i.e. $f_1(\sigma^c) = 0$, $\tilde{J} = \tilde{J}(\sigma^c)$, $\tilde{I} = \tilde{I}(\sigma^c)$, $f_2(\sigma^c) = 0$ and $f_3(\sigma^c) = 0$.

## 3. PLASTICITY FORMULATION

### 3.1 Yield Surfaces

In the plasticity model developed herein, the envelope of failure surfaces $f_1(\sigma^c)$ and $f_2(\sigma^c)$ are used as the yield surface. Although (4) represents incipient elastic buckling, it is assumed that elastic buckling precipitates plastic hinge growth and plastic deformation occurs almost immediately after buckling. Experimental data (Triantfillou et. al., 1989) at yielding is shown in Fig. 3 along with the proposed failure surfaces. Assuming transverse isotropy with the 1 axis as the axis of symmetry, the following parameters were used to model the data for the 196 kg/m$^3$ foam ($\rho_{rel} = 0.16$) shown:

---

[1]Eq. 34 in Gibson et. al. (1989) is stated $\pm\sqrt{\tilde{J}} + a\,\tilde{I}^2 - 1 = 0$. The $\pm$ is not necessary since the positive always controls.

$k_{11} = 3.3$ MPa, $k_{22} = k_{33} = 2.2$ MPa,
$f_1(\sigma^c) \Rightarrow a = 0.09\ \rho_{rel} = 0.0144$,
$f_2(\sigma^c) \Rightarrow h = 5$ MPa, $R^2 = 7.5$

For the transverse isotropic foam, a shear tests must be made in the isotropic plane to obtain the $k_{23}$ term and in the normal plane to determine the $k_{12} = k_{31}$ term. For an isotropic foam, $k_{ij} = k\delta_{ij}$. Typically the plastic hinge surface controls the uniaxial compression yield as shown in Fig. 3. Furthermore 'a' is always small in (1) such that the uniaxial yield stress in the i direction is given by $(\sigma^c_{ii})^{yield} \approx k_{ii}$ (no sum). Triantafillou et. al. (1989) show additional results that can be used to verify the yield surfaces $f_1$ and $f_2$ for biaxial loading and foams of different density. Although Patel and Finnie (1969), Shaw and Sata (1966), and Zaslawsky (1972) approximately fit biaxial data using a principle stress criterion, it was shown by Triantafillou (1989) that the yield surface $f_1(\sigma^c)$ would also fit the same biaxial data. A principle stress yield surface would not provide a good fit of the triaxial data from Triantafillou (cf. Fig. 3) in the compression-tension quadrants.

## 3.2 Elasto-Plasticity

The commonly assumed additive split of the rate of deformation tensor into elastic and plastic parts is assumed; i.e. $\mathbf{d} = \mathbf{d}^e + \mathbf{d}^p$. Strict physical justification for this assumption is not available; it is adopted mainly for utilitarian reasons. The elastic stress is due to bending and axial deformation of the cellular walls and is given by:

$$\overset{\nabla}{\sigma}{}^c = \mathbf{C}^c : \mathbf{d}^e \qquad (7)$$

where $\overset{\nabla}{\sigma}{}^c$ is some objective stress flux (e.g. Jaumman rate) and $\mathbf{C}^c$ is the fourth order stiffness tensor for the cells. In general, $\mathbf{C}^c$ is orthotropic and requires its own evolution (rate) equation to account for material rotation.

At large strains the foam can become 100-1000 times stiffer than $\mathbf{C}^c$. A standard plasticity formulation with a hardening law given for $f_1(\sigma^c)$ and $f_2(\sigma^c)$ and Eq. (7) can not provide enough stiffness when using realistic material constants. Instead, all the hardening is accounted for by the densification stress $\sigma^d$ in a total strain plasticity formulation as will be seen. The additive spit of the stress tensor given by (6) provides a convenient way to incorporate the large amount of hardening necessary in a foam model.

## 3.3 Flow Law

All experimental results indicate that very little transverse deformation occurs when a foam specimen in uniaxial compression is yielding (Shaw and Sata, 1966; Patel and Finnie, 1969; Gibson and Ashby 1982; Nielsen et. al., 1987 and 1993). For example, Fig. 4 shows the lateral strain plotted against the longitudinal strain from a uniaxial compression test of a rigid polystyrene. (Shaw and Sata, 1966). This zero "plastic Poisson's ratio" is a particularly important characteristic. Whereas a nearly incompressible material such as steel stiffens from confinement (e.g. plane strain conditions), a foam would not experience stiffening in confined conditions; technologically, this is what makes foams very useful for impact protection. An associative flow law using the yield surfaces $f_1(\sigma^c)$ and $f_2(\sigma^c)$, though appealing from a stability point of view, would provide nearly incompressible material response. To circumvent this, the following non-associative flow law is proposed for isotropic foams:

$$\mathbf{d}^p = \dot{\gamma}\sigma^c \qquad (8)$$

where $\dot{\gamma}$ is a consistency parameter used to maintain the constraint of the yield surfaces. An orthotropic version of (8) is given in Section A.1 of the Appendix. With (8), no out-of-plane plastic strain will occur under plane stress conditions (i.e. uniaxial compression).

One disadvantage of using a non-associative flow law is that symmetry of the elasto-plastic tangent stiffness is lost. This non-symmetry poses both theoretical and practical numerical problems. Under small strain conditions using an associative flow law, the stress field is unique for given boundary

conditions as long as no plastic softening occurs. To ensure uniqueness of the stress state with a non-associative flow law, a certain amount of hardening must be added. Raneicki (1979) provided the lower bound for the rate of hardening that would be sufficient to guarantee uniqueness with a non-associative flow law. It can be shown that using this bound would provide far to much hardening than is realistic for this material since the material often behaves almost perfectly plastic for strains up to 40%. Due to this issue, the notion of the densification stress was introduced in the model. Using this idea the model tentatively appears to behave well under the loading conditions tested even though Raneicki's condition is not met. Although the non-associative flow laws do not satisfy maximum dissipation/associativity, as prescribed by Il'usion's postulate, the model here can be shown to satisfy the Clausius-Duhem inequality (positive dissipation) for small strains.

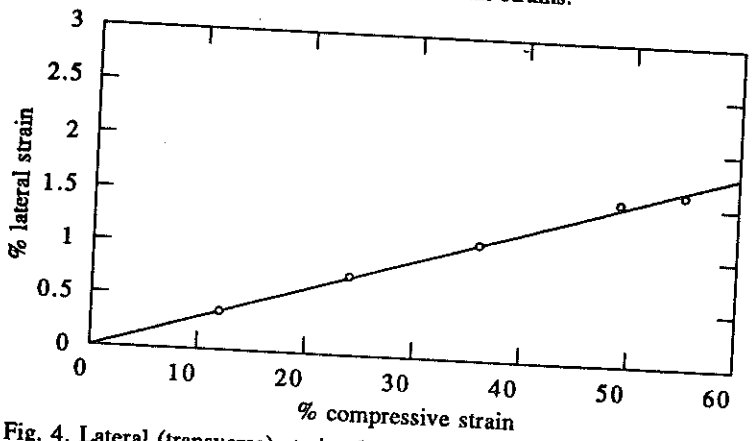


Fig. 4. Lateral (transverse) strain plotted versus compressive strain from a uniaxial compression test of polystyrene (Shaw and Sata, 1966).

### 3.4 Consistency Conditions

The two yield surfaces are restated for convenience in (9) and (10) and shown plotted in invariant space in Fig. 5.

$$f_1(\sigma^c) = \sqrt{\bar{J}} + a\,\bar{I}^2 - 1 = 0 \tag{9}$$

$$f_2(\sigma^c) = \bar{J} + \frac{1}{R^2}\left(\bar{I}^2 - h^2\right) = 0 \tag{10}$$

Given (9) and (10), the value of $\bar{I}$ at which the surfaces intersect is calculated to be:

$$\bar{I}^{int} = -\left[\frac{(2aR^2 - 3) + \left[(2aR^2 - 1)^2 + 4a^2R^2(h - R^2)\right]^{1/2}}{a^2R^2}\right]^{1/2} \tag{11}$$

where $\bar{I}^{int}$ is in compression.

It is necessary to determine the conditions of plastic loading and unloading. From (7) and (8), the rates change of (9) and (10) are given by:

$$\dot{f}_\alpha(\sigma^c) = \frac{\partial f_\alpha}{\partial \sigma^c} : C^c : \mathbf{d} - \dot{\gamma}\frac{\partial f_\alpha}{\partial \sigma^c} : C^c : \sigma^c = 0 \quad (\alpha = 1,2) \tag{12}$$

For an isotropic foam (see Section A.2 of the Appendix for orthotropic case), the following quantities are always greater than zero for a non-trivial stress state:

$$\frac{\partial f_1}{\partial \sigma^c} : C^c : \sigma^c = 2a\,(3\lambda + 2\mu)\,\bar{I}^2 + 2\mu\sqrt{\bar{J}} > 0 \tag{13}$$

$$\frac{\partial f_2}{\partial \sigma^c} : C^c : \sigma^c = \frac{1}{R^2}\,(3\lambda + 2\mu)\,\bar{I}^2 + 4\mu\bar{J} > 0 \tag{14}$$

where $\lambda$ and $\mu$ are the Lamé parameters for an isotropic material in this framework. Loading for a surface $\alpha$ is said to be active under the following conditions:

$$f_\alpha(\sigma^c) = 0 \text{ and } \frac{\partial f_\alpha}{\partial \sigma^c} : C^c : d > 0 \tag{15}$$

To maintain the constraint $f_\alpha(\sigma^c) = 0$ under active loading, Eq. (12) is solved for the consistency parameter $\dot{\gamma}$ giving:

$$\dot{\gamma} = \frac{\partial_{\sigma^c} f_\alpha : C^c : d}{\partial_{\sigma^c} f_\alpha : C^c : \sigma^c} \tag{16}$$

From Eqs. (13), (14) and (15), $\dot{\gamma} > 0$ for active loading. The following three cases determine the value of the consistency parameter:

(i) Loading is not active for either surface $\dot{\gamma} = 0$.
(ii) Loading is active for just one of the surfaces say $f_1$, then $\dot{\gamma} = \partial_{\sigma^c} f_1 : C^c : d / \partial_{\sigma^c} f_1 : C^c : \sigma^c$
(iii) If both surfaces are active then $\dot{\gamma} = \max(\partial_{\sigma^c} f_\alpha : C^c : d / \partial_{\sigma^c} f_\alpha : C^c : \sigma^c ; \alpha = 1,2)$

In case (iii), if $\alpha = 1$ provides the maximum value, then the stress state will satisfy $f_1(\sigma^c) = 0$ and $f_2(\sigma^c) < 0$. Koiter's rule is not observed in this model since only one flow direction is respected. From (7) and (8) the stress rate is given by:

$$\overset{\nabla}{\sigma}{}^c = C^c : (d - \dot{\gamma}\sigma^c) \tag{17}$$

Assuming that **d** is given, the appropriate consistency parameter is chosen based on one of the above three conditions and substituted in (17). The elastoplastic tangent moduli are then given by the expression

$$C^{ep} = \begin{cases} C^c & \text{if } \dot{\gamma} = 0 \\ C^c - \dfrac{[C^c : \sigma^c] \otimes [C^c : \partial_{\sigma^c} f_\alpha]}{\partial_{\sigma^c} f_\alpha : C^c : \sigma^c} \; (\alpha = 1 \text{ or } 2) & \text{if } \dot{\gamma} > 0 \end{cases} \tag{18}$$

The value of $\alpha$ in (18) is chosen based on the criterion given in cases (ii) and (iii) above.

## 3.5 Discrete Formulation

Before presenting the densification/hardening model and the viscous regularization of the overall model, a brief description is given of an algorithmic version of the model as presented so far. The setting for this algorithmic version is the standard strain driven context of a finite element program where the constitutive routines are designed to compute "new" stresses for given strain increments based on "old" stress and history variables.

An implicit backward Euler difference scheme is used in integrating Eq. (8) such that the increment in plastic strain $\Delta\varepsilon^p = d^p \Delta t$ from time $t_n$ to time $t_{n+1}$ is given by:

$$\Delta\varepsilon^p = \gamma \sigma^{c\,(n+1)} \tag{19}$$

To simplify notation, we have defined $\gamma = \dot{\gamma}\Delta t$ . The superscript (n+1) indicates quantities evaluated at time $t_{n+1}$. Substituting Eq. (19) into (17) and assuming all quantities are referred to the co-rotating coordinate system such that $\overset{\nabla}{\sigma}{}^c$ can be replaced by $\dot{\sigma}^c$ gives the following classical stress update

$$\begin{aligned} \sigma^{c\,(n+1)} &= \sigma^c_{trial} - \gamma\, C^c : \sigma^{c\,(n+1)} \\ \sigma^c_{trial} &= C^c : \Delta\varepsilon + \sigma^{c\,(n)} \end{aligned} \tag{20}$$

where $\Delta\varepsilon = \mathbf{d}\,\Delta t$ and $\sigma^c_{trial}$ is the elastic trial stress. To make the above equations meaningful, $\gamma$ must be determined from a consistency condition.

Assuming isotropy[2] equation $(20)_1$ is inverted to give

$$\sigma^{c\,(n+1)} = [\alpha(\gamma)\, \mathbf{1}\otimes\mathbf{1} + \beta(\gamma)\, \mathbf{I}] : \sigma^c_{trial} \tag{21}$$

---

[2]The following development assumes isotropy. It can be easily generalized to the orthotropic case especially in view of the restriction of the elasticity tensor $C^c$ to the diagonal form given the Appendix.

where $\mathbf{I}$ is the symmetric rank four identity tensor, $\mathbf{1}$ is the second order identity and $\alpha$ and $\beta$ are defined by

$$\alpha(\gamma) = \frac{-\gamma\lambda}{(2\mu\gamma+1)(2\mu\gamma+1+3\gamma\lambda)}$$
$$\beta(\gamma) = \frac{1}{2(2\mu\gamma+1)} \tag{22}$$

Substituting (21) and (22) into (2) and (3) provides the following updates for the stress invariants

$$\sqrt{\bar{J}^{n+1}} = 2\beta(\gamma)\sqrt{\bar{J}_{trial}} \qquad \bar{I}^{n+1} = [3\alpha(\gamma)+2\beta(\gamma)]\bar{I}_{trial} \tag{23}$$

where $\bar{J}^{n+1} = \bar{J}(\sigma^{c\,(n+1)})$ , $\bar{J}_{trial} = \bar{J}(\sigma^{c}_{trial})$ , and $\bar{I}_{trial} = \bar{I}(\sigma^{c}_{trial})$ . Eqs. (23) can be substituted into Eqs. (9) and (10) to give:

$$f_1(\sigma^{c\,(n+1)}) = 2\sqrt{3}\beta(\gamma)\sqrt{\bar{J}_{trial}} + a\,(3\alpha(\gamma)+2\beta(\gamma))\,\bar{I}^2_{trial} - 1$$
$$f_2(\sigma^{c\,(n+1)}) = 4\beta(\gamma)^2\bar{J}_{trial} + 1/R^2\,[(3\alpha(\gamma)+2\beta(\gamma))\,\bar{I}^2_{trial} - h^2] \tag{24}$$

In a finite element formulation at time $t_{n+1}$ the strain increment is given and the trial stress is used to calculate Eqs. $(24)_1$ and $(24)_2$. If either are greater than zero, a Newton-Raphson algorithm is used to find the value of $\gamma$ necessary to satisfy $f_1(\sigma^{c\,(n+1)}) = 0$ and or $f_2(\sigma^{c\,(n+1)}) = 0$ [3]. In the case where both $(24)_1$ and $(24)_2$ are greater than zero, the larger of the two values of $\gamma$ necessary to satisfy the constraints is used. It can be shown that the return map given by (23) provides a unique point $(\bar{I}^{n+1}, \bar{J}^{n+1})$ on the envelope of the two yield surfaces. Furthermore this point corresponds to a single value of $\gamma$. Solving (9) and (10) for the square root of $\bar{J}$ gives:

$$\sqrt{\bar{J}} = 1 - a\,\bar{I}^2 \qquad \sqrt{\bar{J}} = \frac{1}{R}\left[h^2 - \bar{I}^2\right]^{1/2} \tag{25}$$

Restating (23) gives,

$$\sqrt{\bar{J}^{n+1}} = \frac{\sqrt{\bar{J}_{trial}}}{2\mu\gamma+1}, \qquad \bar{I}^{n+1} = \frac{\bar{I}_{trial}}{2\mu\gamma+1}\left[1 - 3\lambda\gamma/(2\mu\gamma+3\lambda\gamma+1)\right] \tag{26}$$

It is seen that $\bar{I}^{n+1}$ is a single valued function of $\gamma$ such that $(26)_2$ is invertible:

$$\gamma = \frac{\bar{I}_{trial}/\bar{I}^{n+1} - 1}{3\lambda + 2\mu} \tag{27}$$

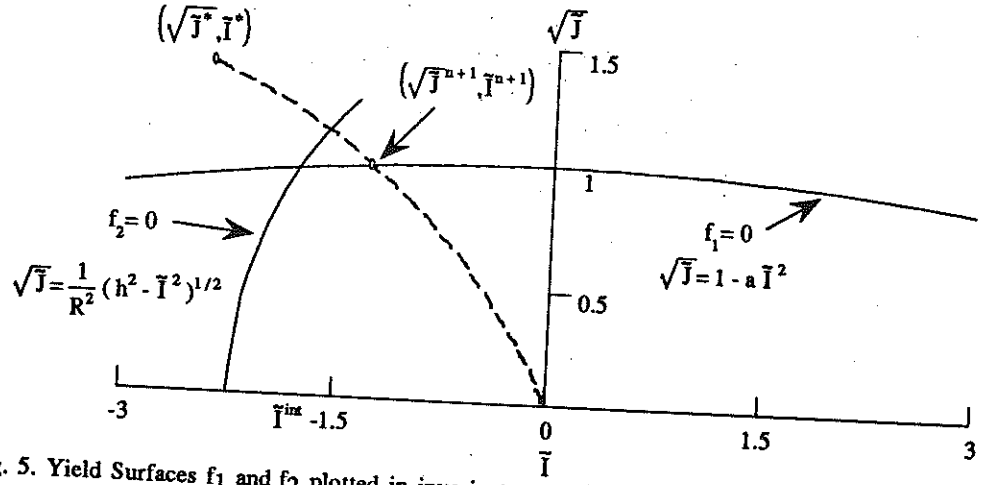


Fig. 5. Yield Surfaces $f_1$ and $f_2$ plotted in invariant space. The dashed curve shows parametric path traversed by Eqs. $(26)_1$ and $(26)_2$.

[3] These equations can be solved in closed form but involve solutions to a cubic equation which are unwieldy.

From (26) it is also seen that both $\tilde{I}^{n+1}$ and the square root of $\tilde{J}^{n+1}$ approach zero asymptotically as $\gamma$ goes from 0 to infinity. This is illustrated schematically in Figure 5 where the parametric path of $\tilde{I}^{n+1}$ and $\tilde{J}^{n+1}$ is shown (long dashed line). If $\tilde{I}_{trial}$ is negative, then $\tilde{I}^{n+1}$ is always increasing and $\tilde{J}^{n+1}$ is always decreasing as $\gamma$ goes from 0 to infinity. Whereas examination of $(25)_1$ and $(25)_2$ shows that the square root of $\tilde{J}$ always increases with increasing $\tilde{I}$ for $\tilde{I} < 0$. Therefore (26) may only intersect either yield surface (25) once corresponding to the single value of $\gamma$ given by (27). A similar argument is made when $\tilde{I}_{trial}$ is positive. If $\tilde{I}_{trial}$ is zero, then $(24)_1$ and or $(24)_2$ may be solved for zeroes by solving a linear equation in $\gamma$.

### 3.6 Hardening Law

As mentioned in Section 2, it is assumed that the majority of the hardening in the foam is due to contact of the cell walls. In theory the foam becomes as stiff as the parent material when the free volume diminishes. A convenient way to incorporate hardening is to uncouple the stress into stress due to cell wall deformation and stress due to cell wall contact: $\boldsymbol{\sigma} = \boldsymbol{\sigma}^c + \boldsymbol{\sigma}^d$. The following evolution equation is used for the densification/hardening stress

$$\overset{\nabla}{\boldsymbol{\sigma}}{}^d = f(c,\varepsilon^{vd},\varepsilon^v)\, \mathbf{C}^d : \mathbf{d} \tag{28}$$

where $\varepsilon^v = \int_t d_{ii}\, dt = \ln(J)$, J is the Jacobian determinant of the deformation gradient, and $\mathbf{C}^d$ is the isotropic tensor representing the stiffness of the fully solidified foam. The function $f(c,\varepsilon^{vd},\varepsilon^v)$ is given by:

$$f(c,\varepsilon^{vd},\varepsilon^v) = \begin{cases} 0 & \varepsilon^v \geq 0 \\ \dfrac{\tan^{-1}(c\,\varepsilon^{vd}) + \tan^{-1}(c\,(\varepsilon^v - \varepsilon^{vd}))}{\tan^{-1}(c\,\varepsilon^{vd}) - \pi/2} & \varepsilon^v \leq 0, \dot{\varepsilon}^v \leq 0 \end{cases} \tag{29}$$

where c is the rate of densification, $\varepsilon^{vd} = \ln(J^d)$ and $J^d$ is the relative volume at which "lockup" or full densification occurs. The function $f(c,\varepsilon^{vd},\varepsilon^v)$ varies from 0 at $\varepsilon^v = 0$ to 1 at $\varepsilon^v \approx \varepsilon^{vd}$ as seen from Fig. 6. Assuming Poisson's effects are negligible, for a 1-D compression test the densification/hardening model predicts a stress along the compression axis of

$$\sigma_{11} = \sigma^c_{11} - E^d \frac{2c\ln(\lambda/\lambda^d)\left[\tan^{-1}(c\ln\lambda^d) + \tan^{-1}(c\ln(\lambda/\lambda^d))\right] + \ln\left[\dfrac{1+c^2\ln^2(\lambda/\lambda^d)}{1+c^2\ln^2(\lambda^d)}\right]}{2c\,(\tan^{-1}(c\ln\lambda^d) - \pi/2)} \tag{30}$$

where $\mathbf{C}^d = E^d\,\mathbf{I}$ has been assumed in (28), $\lambda$ is the uniaxial stretch ($\lambda < 1$ for compression), and $\lambda^d = J^d$ is the lockup stretch. The uniaxial stress is plotted for three values of c in Fig. 7. The family of curves in Figure 7 are typical of curves seen in uniaxial experimental tests (Gibson and Ashby, 1988). Fits to experimental data are simple since the yield stress $(\sigma^c_{11})^{yield}$ and lock up stretch $\lambda^d$ are usually obvious. The modulus $E^d$ is usually close to the modulus of the solid material. The value of c can be found easily by trial and error or systematic property identification.

When unloading occurs ($\varepsilon^v < 0, \dot{\varepsilon}^v > 0$) the material retains its stiffness from the loading phase. For example, if unloading occurs at $\varepsilon^v = \varepsilon^*$ then $f(\varepsilon^v) = f(\varepsilon^*)$ for all $\varepsilon^v < \varepsilon^*$ until the material reloads to the strain $\varepsilon^*$ at which $f(\varepsilon^v)$ then varies according to (29). This loading/unloading path is shown in Fig. 8 for uniaxial compression. Typically these materials are not subject to large strain cyclic loading. For those conditions a more appropriate evolution equation for unloading would be required.

Experimental results of orthotropic foams (Maji, et. al., 1991; Patel and Finnie, 1969) show that the rate of densification c is related to the orientation of the foam. A modified version of (28) is proposed for an orthotropic foam:

$$\overset{\nabla}{\boldsymbol{\sigma}}{}^d = \mathbf{f}(c,\varepsilon^{vd},\varepsilon^v) : \mathbf{C}^d : \mathbf{d} \tag{31}$$

where the function $\mathbf{f}(\mathbf{c},\varepsilon^{vd},\varepsilon^v)$ is a fourth order tensor and $\mathbf{c}$ is a vector. In Voigt matrix notation, for example, one could take the function $\mathbf{f}(\mathbf{c},\varepsilon^{vd},\varepsilon^v)$ in the corotating coordinate system as the diagonal matrix given by

$$\mathbf{f}(\mathbf{c},\varepsilon^{vd},\varepsilon^v) = \mathrm{diag}\{\, f_1, f_2, f_3, (f_1+f_2)/2, (f_2+f_3)/2, (f_3+f_1)/2\} \tag{32}$$

using the notation $f_i = f(c_i, \varepsilon^{vd}, \varepsilon^v)$.

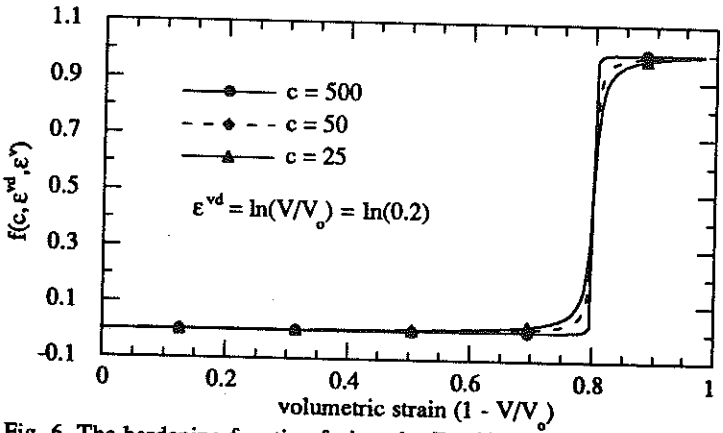


Fig. 6. The hardening function f given by Eq. 29. Specific form of f causes the stiffness to reach fully densified state near volumetric lockup strain $\varepsilon^{vd} = \ln(V/V_o)$.

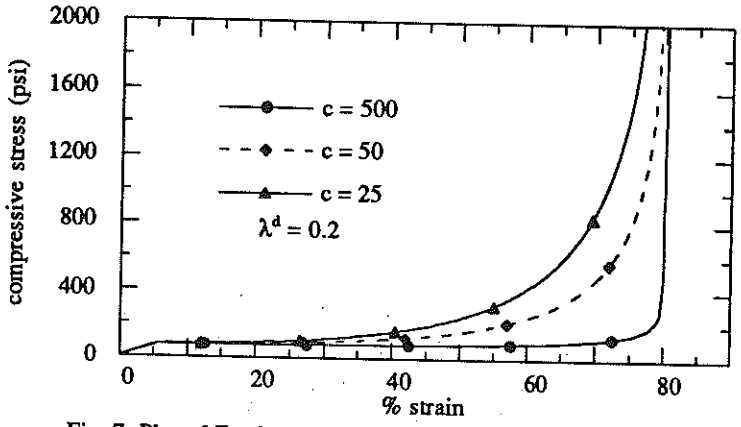


Fig. 7. Plot of Eq. 30 using different values of the hardening rate c.

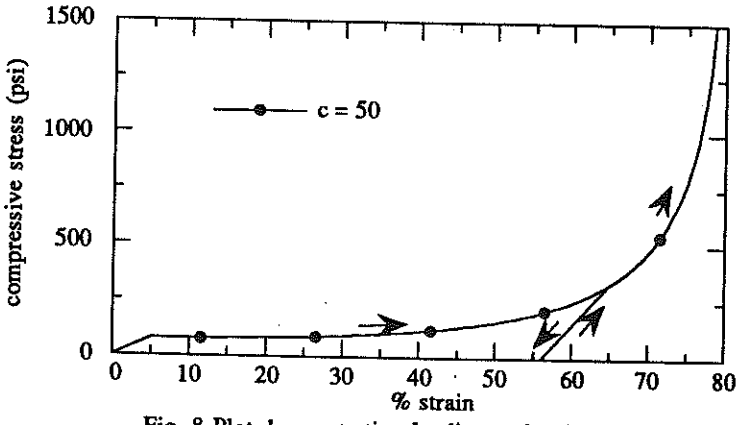


Fig. 8 Plot demonstrating loading and unloading path.

## 3.7 Viscoplasticity

Rate dependence of the foam is due to the viscoplastic behavior of the solid matrix and the resistance of air flow through the cellular structure. Nagy et. al. (1974) compares experimental data from drop tests performed on open cell foams in a partial vacuum to tests done at atmospheric pressure. The results show that air flow is a factor but its effects were not substantial compared to the solid. Here it is assumed that most of the rate dependence is due to the bending and stretching of the cell walls represented by the stress $\sigma^c$ .

The Perzyna-type viscoplasticity models are often used to characterized such behavior with flow laws of the form

$$\mathbf{d}^{vp} = \frac{\langle f(\sigma) \rangle}{\eta} g(\sigma) \tag{33}$$

where f is the yield function, $\langle\ \rangle$ are the Macauley brackets, $\eta$ is the fluidity parameter and g is the flow direction. When multisurface yield criterion are used it is known that such models are inappropriate and Duvaut-Lions type models must be used (Simo et. al. 1988). Duvaut and Lions (1972) proposed the following type of flow law for single surface viscoplasticity

$$\mathbf{d}^{vp} = \frac{1}{\eta} C^{-1} : (\sigma - \sigma_{proj}) \tag{34}$$

where $\eta$ is the fluidity parameter, $C^{-1}$ is the inverse of the elastic stiffness matrix and $\sigma_{proj}$ is the projection of the stress $\sigma$ onto the elastic domain given by the yield surfaces. When $\sigma$ is within the elastic domain $\mathbf{d}^{vp} = 0$. As shown by Simo et. al. (1988) this formulation can be used for multisurface plasticity where the elastic domain is given by the envelope of several intersecting yield surfaces. In Simo et. al. (1988), the projected stress $\sigma_{proj}$ is found using the closest point projection algorithm given for associative flow. Here the return mapping described in Section 3.5 is used to find the projected stress.

The following strain dependent power law version of the flow law (34) is proposed for the isotropic multisurface model developed here

$$\mathbf{d}^{vp} = \frac{\| \sigma^c - \sigma^c_{proj} \|^{n-1}}{J \eta} C^{c-1} : (\sigma^c - \sigma^c_{proj}) \tag{35}$$

where $\| \sigma \|^2 = \sigma : \sigma$ and $\eta$ and n are experimentally determined parameters. An orthotropic version of (35) which is analogous to Eq. A.1 is considered in Section A.3 of the Appendix. Substitution of (35) into (7) provides the evolution equation for viscoplastic loading

$$\dot{\sigma}^c + \frac{\| \sigma^c - \sigma^c_{proj} \|^{n-1}}{J \eta} (\sigma^c - \sigma^c_{proj}) = C^c : \mathbf{d} \tag{36}$$

Again, Poisson's effects are typically not considerable for the foam; therefore, assuming a diagonal form for $C^c$ and uniaxial compression in the 1 direction in Eq. (36) gives

$$\dot{\sigma}^c_{11} + \frac{1}{J \eta} (\sigma^c_{11} - k_{11})^n = E^c d_{11} \tag{37}$$

where the approximation for the yield stress $(\sigma^c_{11})^{yield} \approx k_{11}$ can be made for uniaxial compression since 'a' in Eq. (1) is usually small. Furthermore, because there is no transverse deformation occurring $J = \lambda$ where $\lambda$ is the uniaxial stretch. The strain rate $d_{11} = \dot{\lambda} / \lambda$ where $\dot{\lambda}$ is the stretch rate. For a uniaxial compression test at constant stretch rate, Eq. (37) reaches a steady state such that $\dot{\sigma}^c_{11} = 0$ and

$$\sigma^c_{11} = k_{11} + (\eta E^c \dot{\lambda})^{1/n} \tag{38}$$

Had J not been included in (35), the foam would stiffen in compression at constant stretch rate since the strain $d_{11} = \dot{\lambda} / \lambda$ would increase as $\lambda$ became small. This is not seen in experimental results for rigid polymeric foams (Patel and Finnie, 1969; Gibson and Ashby, 1988). By including the Jacobian determinant in the denominator of Eq. (35) this spurious effect has been avoided.

# 4. APPLICATIONS

## 4.1 Finite Element Implementation

The constitutive model presented in Section 3 was implemented in the explicit finite element code DYNA3D (Whirley and Englemann, 1993). Polymeric foams are often used in interior components of automobiles as crash padding and are therefore an important modeling aspect in vehicle crash simulation. Explicit codes such as DYNA3D are usually the preferred method of analysis for these situations. Because extremely small times steps are used in explicit codes, the tangent stiffness matrix is not needed and the viscoplastic formulation presented in Section 3.7 was implemented in an explicit form without complications due to instability. It is mentioned, however, that the above algorithms can be exactly linearized to form a non-symmetric algorithmic tangent for use in implicit codes.

## 4.2 Drop Test

High speed drop tests are typically performed to evaluate a foam's response under crash conditions. A drop test (Rossio, et. al.,1992) was performed on the 3 pcf polyurethane foam shown statically loaded in Fig. 1 by dropping a 40 lb. flat 6 in. radius cylindrical aluminum plate onto a 2.5 in. thick 10x10 in. square specimen at 15.5 mph and 20.3 mph. The foam was treated as isotropic and the following material properties were used to simulate foam response for the three experiments:

Material parameters for cell walling bending and stretching
$C^c \Rightarrow$ modulus of elasticity $E^c$ = 600 psi, Poisson's Ratio $\nu^c$ = 0.0
yield parameter k = 30 psi,
$f_1(\sigma^c)$. $\Rightarrow$ a = 0.0042
$f_2(\sigma^c) \Rightarrow$ h = 90 psi, R = 9.0

Material parameters for densification
$C^d \Rightarrow$ modulus of elasticity $E^d$ = 4100 psi, Poisson's Ratio $\nu^d$ = 0.0

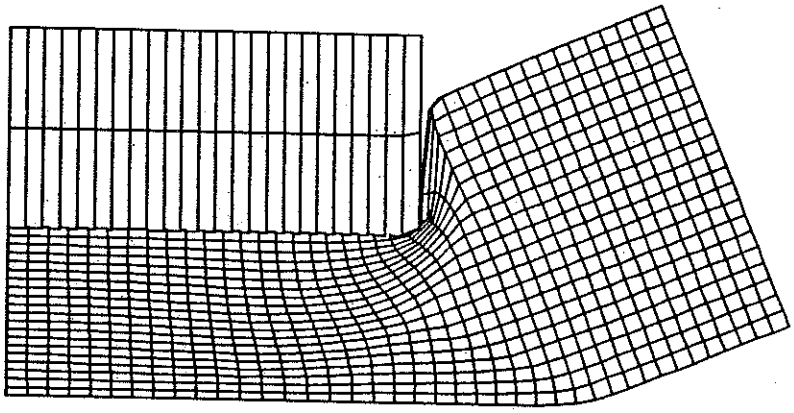

Fig. 9. One half of the deformed mesh from DYNA3D showing a foam block (fine mesh) being crushed by a 40 lb. flat ended aluminum cylinder (coarse mesh) in a 15.5 mph drop test. At this point the foam block has deformed by 50% underneath the aluminum cylinder.

For simplicity, the foam was modeled as plane strain. This is also effectively plane stress because of the zero Poisson's ratio. In Fig. 9 one half of the cross section of the model is shown after the aluminum plate has penetrated 1.25 in. (50% deformation) into the foam. A slide surface was used on all sides of the aluminum plate (course mesh) to provide contact at the foam interface. A rigid wall was

used as an interface at the bottom of the foam to allow gaps to develop as seen in the right corner of the foam in Fig. 9. Acceleration of the aluminum block was measured and used to calculate the average stress exerted by the foam. Figures 10 and 11 show the average stress response from the 15.5 and 20.3 mph experiments. The foam material did not appear to be very rate dependent as is sometimes the case. The most prominent feature in the 20.3 mph experiment is the extreme stiffening from densification. It is seen that the model simulation overshoots the maximum stress given by the 20.3 mph experiment. This could have been somewhat alleviated had a curve fitting technique been used. Furthermore, tensile softening due to matrix cracking should be added to alleviate the bending seen in Fig. 9.

Models which only include hardening due to volumetric strain (Nielsen, 1993) of the trapped pore fluid behave incompressibly at high strains and unload nearly elastically. These effects are usually not seen from experiments. Typically the material unloads at a higher rate than an elastic material as seen in Figs. 10 and 11.

### 4.3 Uniaxial Tests on Rate Dependent Orthotropic Foam

Low density polymeric foams are often highly orthotropic and rate dependent. A uniaxial compression test was performed (Patel and Finnie, 1969) on a 3.1 pcf polyurethane foam at four different rates and two different orientations with the results shown in Figures 12 and 13. Assuming transverse isotropy with the axis of symmetry in the 1 direction, the following parameters were used to simulate the experimental results

Material parameters for cell wall bending and stretching
$C^c \Rightarrow E^c_{11} = 1200$ psi, $E^c_{22} = E^c_{33} = 746.2$ psi
yield parameters $k_{11} = 36$ psi, $k_{22} = k_{33} = 22.386$ psi
$k_{23} = k_{31} = 29$ psi, $k_{23} = 22.386$ psi
$f_1(\sigma^c) \Rightarrow a = 0.0044$
$f_2(\sigma^c) \Rightarrow h = 90$ psi, $R = 9.0$
rate dependent parameters $\Rightarrow \eta = 0.3881$, $n = 10.742$

Material parameters for densification
$C^d \Rightarrow$ modulus of elasticity $E^d = 25000$ psi, Poisson's Ratio $\nu^d = 0.0$
$c \Rightarrow c_{11} = 800$, $c_{22} = c_{33} = 200$

The ratio of yield stress to stiffness for the different orientations is typically constant (Patel and Finnie, 1969). such that $\zeta = k_{11} / E^c_{11} = k_{22} / E^c_{22} = 0.03$

The results shown in Fig. 12 are uniaxial compression at different loading rates in the 1 direction (foam rise direction). As mentioned previously, the stress reaches a steady state at which equations such as (38) and (A.15) can be used to characterize the response. This steady state is typical in low density foams (Gibson and Ashby, 1988). Experimental data from Sherwood (1992) shows some additional hardening at higher strains as the rate of loading is increased. This effect could be captured by replacing the Jacobian determinant J in the flow law (35) and (A.14) with $\alpha + \beta J$ such that the amount of strain rate dependent hardening could be adjusted by adjusting material constants $\alpha$ and $\beta$.

The results shown in Fig. 13 are for uniaxial compression in the 1 direction (foam rise direction) and 2 direction. Clearly the material hardens at a higher rate in the 2 direction. This effect has been seen in other experimental results (Maji, et. al., 1991). The effect is probably due to the cell shape ratios (Huber and Gibson, 1988). The foam cells are longer and thinner in the foam rise direction such that contact of cell walls occurs sooner when loading is perpendicular to this rise direction. Use of the orthotropic hardening law (30) appears to be effective in capturing the hardening seen in Fig. 13.

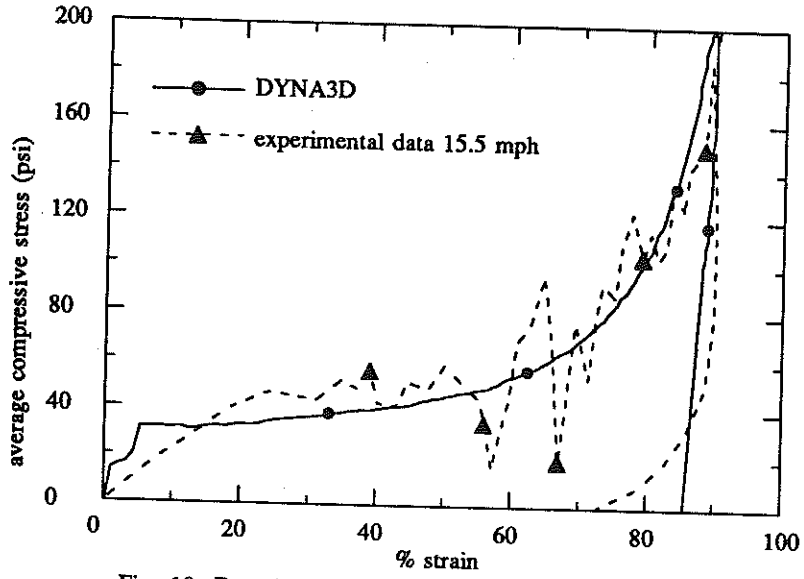


Fig. 10. Experimental results from drop test (Rossi et. al. 1992) for 3 pcf polyurethane foam at 15.5 mph along with DYNA3D simulation.

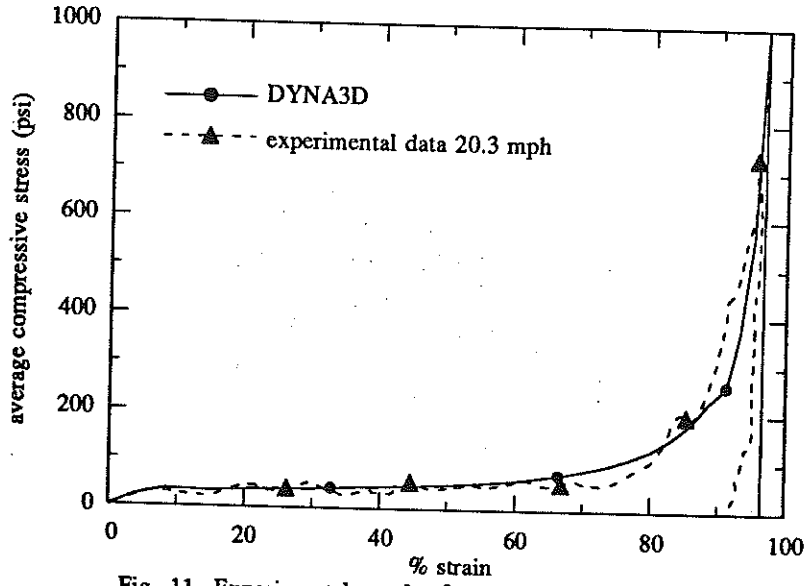


Fig. 11. Experimental results from drop test (Rossi et. al. 1992) for 3 pcf polyurethane foam at 20.3 mph along with DYNA3D simulation.

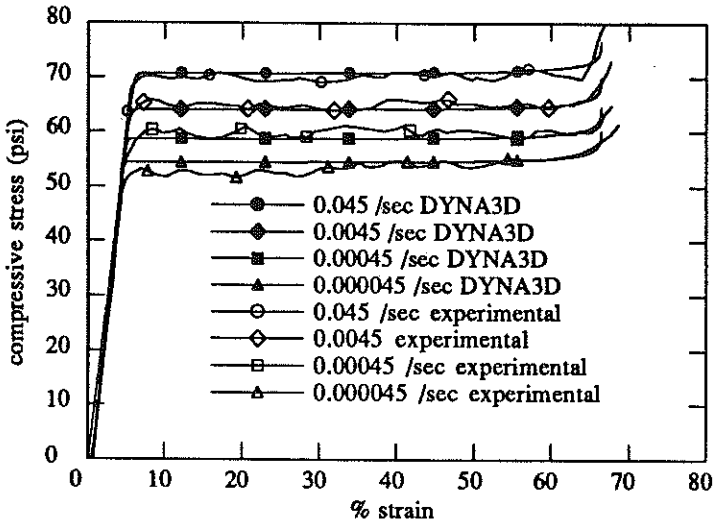


Fig. 12. Uniaxial compression test data (Patel and Finnie, 1966) for 3.1 pcf foam at four different stretch rates along with DYNA3D simulation

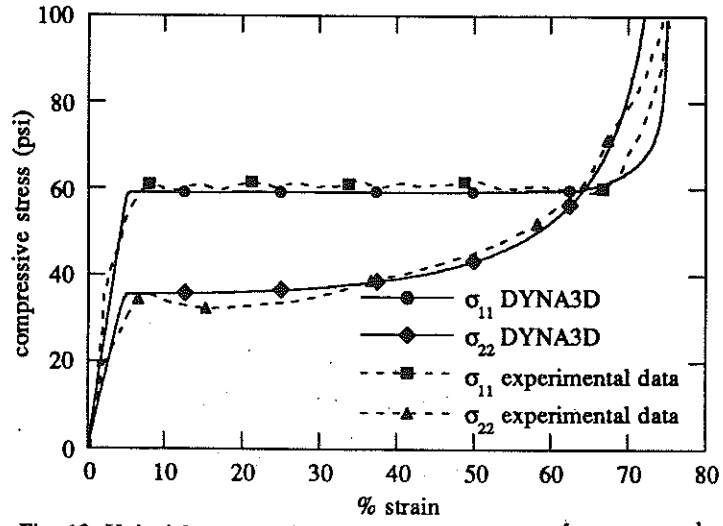


Fig. 13. Uniaxial compression test data at strain rate $\dot{\lambda} = 0.00045\,s^{-1}$ (Patel and Finnie, 1966) for 3.1 pcf foam in the 11 direction (foam rise direction) and 22 direction along with DYNA3D simulation.

## 5. CLOSURE

An orthotropic rate independent plasticity and viscoplasticity formulation was developed by extending the work of Gibson et. al. (1989). This was accomplished by formulating an orthotropic flow law and hardening law and using a modified version of the envelope of failure/yield surfaces proposed by Gibson et. al. The flow law was based on the observation that the material develops little or no transverse strain in a uniaxial compression test. The non-associative flow law in addition to the multisurface yield criterion necessitated a special treatment of the consistency and loading/unloading

conditions. A novel orthotropic hardening law and a modified version of the Duvuat-Lions viscoplasticity formulation were shown to successfully simulate experimental results. The model was implemented in the computer code DYNA3D (Whirley and Englemann, 1993) developed and maintained by Lawrence Livermore National Laboratory.

## REFERENCES


Duvaut, G., and Lions, J.L., 1972, *Les Inequations en Mechanique et en Physique*, Dunod Paris.

Gibson, L.J., and Ashby, M.F., 1982, "The Mechanics of Three-Dimensional Cellular Solids", *Proc. R. Soc. Lond.*, **382**, 43.

Gibson, L.J., and Ashby, M.F., 1988, *Cellular Solids: Structure and Properties*, Pergamon Press (Oxford), 147.

Gibson, L.J., Ashby, M.F., Zhang J., and Triantfillou, T.C., 1989, "Failure Surfaces for Cellular Materials under Multiaxial Loads -I. Modelling", *Int. J. Mech. Sci.*, **31**, 635.

Huber, A. T. and Gibson, L. J., 1988, "Anisotropy of Foams", *Journal of Materials Science*, **23**, 3031.

Maji, A.K., Donald, S. and Cone, K., 1991, "Testing of Impact Limiters for Transportation Cask Design", *Materials Research Society Symposium Proceedings*.

Nagy, A., Ko, W.L.and Lindholm, U.S., 1974, "Mechanical Behavior of Foamed Materials Under Dynamic Compression", *Journal of Cellular Plastics*, **10**, 7.

Nielsen, M.K., Morgan, H.S., and Krieg, R.D., 1987, *A Phenomenological Constitutive Model for Low Density Polyurethane Foams*, Sandia National Laboratories, Albuquerque New Mexico, SAND86-2927.

Nielsen, M.K., 1993, *Continuum Representations of Cellular Solids*, Sandia National Laboratories, Albuquerque New Mexico, SAND93-1287

Patel, M.R. and Finnie, I, 1969, *The Deformation and Fracture of Rigid Cellular Plastics under Multiaxial Stress* , Lawrence Livermore National Laboratory, Livermore California, UCRL-13420.

Raniecki, B., 1979, "Uniqueness Criteria in Solids with Non-associated Plastic Flow Laws at Finite Deformations", *Bulletin De L'Academie Polonaise Des Sciences*, **27**, 391.

Rossio, R.C., Vechio M., and Abramczyk, J., 1992, "Polyurethane Energy Absorbing Foams for Automotive Applications", *34th Annual PolyurethaneTechnical/Marketing Conference* , 438.

Shaw, M.C. and Sata, T., 1966, "The Plastic Behavior of Cellular Materials", *Int. J. Mech. Sci.*, **8**, 469.

Sherwood, J.A., 1992, "Constitutive Modeling and Simulation of Energy Absorbing Polyurethane Foam Under Impact Loading", *Polymer Engineering and Science*, **32**, 1138.

Simo, J.C., Kennedy, J.G. and Govindjee, S., 1988, "Non-Smooth Multisurface Plasticity and Viscoplasticity. Loading/Unloading Conditions and Algorithms", *Int. J. Numer. Meth. Engng.*, **26**, 2161.

Triantafillou, T.C., Zhang J., Shercliff T.L., Gibson L.J., and Ashby M.F., 1989, "Failure Surfaces for Cellular Materials under Multiaxial Loads -II. Comparison of Models with Experiment", *Int. J. Mech. Sci.*,**31**, 665.

Whirley, R.G. and Englemann, B., "DYNA3D: A Nonlinear, Explicit, Three-Dimensional Finite Element Code For Solid and Structural Mechanics", University of California, Lawrence Livermore National Laboratory, Rept. UCRL-MA-107254.

Zaslawsky, M., 1972, "Multiaxial-stress Studies on Rigid Polyurethane Foam", *Exper. Mech.*, **2**, 70.

## APPENDIX

### A.1 Orthotropic Flow Law

The following flow law is proposed for orthotropic foams

$$\mathbf{d}^p = \dot{\gamma}\,\tilde{\boldsymbol{\sigma}} \tag{A.1}$$

where

$$\tilde{\boldsymbol{\sigma}} = \mathbf{K}^{-1}:\boldsymbol{\sigma}^c$$

and $\mathbf{K}$ is the fourth order tensor of yield parameters $k_{ij}$ defined in matrix form by

$$\mathbf{K} = \mathrm{diag}(k_{11}, k_{22}, k_{33}, k_{12}, k_{23}, k_{31}) \tag{A.2}$$

Using the stress vector of the form $\boldsymbol{\sigma}^c = \{\sigma^c_{11}, \sigma^c_{22}, \sigma^c_{33}, \sigma^c_{12}, \sigma^c_{23}, \sigma^c_{31}\}^T$ gives

$$\tilde{\boldsymbol{\sigma}} = \left\{\frac{\sigma^c_{11}}{k_{11}}, \frac{\sigma^c_{22}}{k_{22}}, \frac{\sigma^c_{33}}{k_{33}}, \frac{\sigma^c_{12}}{k_{12}}, \frac{\sigma^c_{23}}{k_{23}}, \frac{\sigma^c_{31}}{k_{31}}\right\}^T$$

The flow law given by (A.1) like (8) precludes transverse strain in uniaxial compression. The flow law given by (8) is not used in the orthotropic case for reasons given at the end of Section A.2.

### A.2 Consistency Conditions

During plastic loading the consistency parameter $\dot{\gamma}$ must be greater than zero in order to maintain positive dissipation as required by the Clausius-Duhem inequality and to maintain numerical stability. As shown in Eqs. (12) - (16), the consistency parameter is given by

$$\dot{\gamma} = \frac{\partial_{\sigma^c} f_\alpha : \mathbf{C}^c : \mathbf{d}}{\partial_{\sigma^c} f_\alpha : \mathbf{C}^c : \tilde{\boldsymbol{\sigma}}} \tag{A.3}$$

where $\mathbf{C}^c$ is the orthotropic stiffness tensor. When $f_\alpha(\boldsymbol{\sigma}^c) = 0$ and $\partial_{\sigma^c} f_\alpha : \mathbf{C}^c : \mathbf{d} > 0$ plastic loading is active and the denominator in (A.3) must be positive such that

$$\partial_{\sigma^c} f_\alpha : \mathbf{C}^c : \tilde{\boldsymbol{\sigma}} > 0 \tag{A.4}$$

By definition

$$\tilde{\boldsymbol{\sigma}} = \tilde{\mathbf{S}} + \frac{1}{3}\,\mathrm{tr}\,(\tilde{\boldsymbol{\sigma}})\,\mathbf{1} \tag{A.5}$$

where $\mathbf{1}$ is the second order identity tensor. From (2) and (3) it is seen

$$\tilde{J} = \frac{3}{2}\,\tilde{\mathbf{S}}:\tilde{\mathbf{S}} \qquad \tilde{I} = \mathrm{tr}\,(\tilde{\boldsymbol{\sigma}}) \tag{A.6}$$

Taking the gradients of $f_\alpha(\boldsymbol{\sigma}^c)$ with respect to $\tilde{\boldsymbol{\sigma}}$ gives

$$\frac{\partial f_1}{\partial \tilde{\boldsymbol{\sigma}}} = \frac{3}{2}\frac{1}{\sqrt{\tilde{J}}}\,\tilde{\mathbf{S}} + 2a\tilde{I}\,\mathbf{1} \qquad \frac{\partial f_2}{\partial \tilde{\boldsymbol{\sigma}}} = 3\,\tilde{\mathbf{S}} + \frac{2}{R^2}\tilde{I}\,\mathbf{1} \tag{A.7}$$

Furthermore, from $(A.1)_2$

$$\frac{\partial f_\alpha}{\partial \boldsymbol{\sigma}^c} = \frac{\partial f_\alpha}{\partial \tilde{\boldsymbol{\sigma}}} : \mathbf{K}^{-1} \tag{A.8}$$

Now considering $\alpha = 1$ and substituting (A.5), $(A.7)_1$ and (A.8) into (A.4) gives

$$\frac{\partial f_1}{\partial \boldsymbol{\sigma}^c} : \mathbf{C}^c : \tilde{\boldsymbol{\sigma}} = \left[\frac{3}{2}\frac{1}{\sqrt{\tilde{J}}}\,\tilde{\mathbf{S}} + 2a\tilde{I}\,\mathbf{1}\right] : \mathbf{K}^{-1} : \mathbf{C}^c : \left[\tilde{\mathbf{S}} + \frac{1}{3}\tilde{I}\,\mathbf{1}\right] \tag{A.9}$$

Now a sufficient condition for (A.9) to be always greater than zero is that the stiffness matrix $\mathbf{C}^c$ be proportional $\mathbf{K}$ such that

$$\mathbf{C}^c = \zeta\,\mathbf{K} \qquad \zeta > 0 \tag{A.10}$$

Substitution of (A.10) into (A.9) and contracting gives

$$\frac{\partial f_1}{\partial \boldsymbol{\sigma}^c} : \mathbf{C}^c : \tilde{\boldsymbol{\sigma}} = 2\zeta\left(\frac{1}{2}\sqrt{\tilde{J}} + a\,\tilde{I}^2\right) > 0 \tag{A.11}$$

and similarly

$$\frac{\partial f_2}{\partial \sigma^c}:C^c:\tilde{\sigma} = 2\zeta\,(\tilde{J} + \frac{1}{R^2}\,\tilde{I}^2) \;>0 \tag{A.12}$$

Rewriting (A.10) in matrix form gives

$$C^c = \begin{bmatrix} C_{11} & 0 & 0 & 0 & 0 & 0 \\ 0 & C_{22} & 0 & 0 & 0 & 0 \\ 0 & 0 & C_{33} & 0 & 0 & 0 \\ 0 & 0 & 0 & C_{12} & 0 & 0 \\ 0 & 0 & 0 & 0 & C_{23} & 0 \\ 0 & 0 & 0 & 0 & 0 & C_{31} \end{bmatrix} = \begin{bmatrix} \zeta k_{11} & 0 & 0 & 0 & 0 & 0 \\ 0 & \zeta k_{22} & 0 & 0 & 0 & 0 \\ 0 & 0 & \zeta k_{33} & 0 & 0 & 0 \\ 0 & 0 & 0 & \zeta k_{12} & 0 & 0 \\ 0 & 0 & 0 & 0 & \zeta k_{23} & 0 \\ 0 & 0 & 0 & 0 & 0 & \zeta k_{31} \end{bmatrix} \tag{A.13}$$

A stiffness matrix given by (A.10) and (A.13) is restrictive but nonetheless a reasonable approximation since

a) The Poisson's effects are only observed at small strains and many investigators reported little to no transverse strain in uniaxial compression for all ranges of strain (Nielsen et. al, 1987 and 1990; Shaw and Sata, 1966)

b) Patel and Finnie (1969) and Huber and Gibson (1988) have reported that the ratios of uniaxial stiffness to uniaxial yield stress[4] are near equal for different orientations i.e. $E_{11}/k_{11} \approx E_{22}/k_{22} \approx E_{33}/k_{33}$ for moderately anisotropic foam. For highly anisotropic foams this may not be the case.

Had the flow law been given by (8) instead of (A.1), the sufficient condition for a positive definite consistency parameter would be $C^c = \zeta\,\mathbf{I}$ where I is the identity matrix.

## A.3 Orthotropic Viscoplasticity

The orthotropic version of Eq. (33) is given by

$$\dot{d}^{vp} = \frac{\|\tilde{\sigma} - \tilde{\sigma}_{proj}\|^{n-1}}{J\,\eta}\,C^{c^{-1}}(\sigma - \sigma_{proj}) \tag{A.14}$$

where $(A.1)_2$ is used and $\tilde{\sigma}_{proj} = K^{-1}\,\sigma_{proj}$. When (A.10) is used for the stiffness $C^c$, the flow (A.14) can be shown to be consistent with the rate independent flow law $(A.1)_1$ as $\eta \to 0$. From (A.10), (A.14) and the assumption that 'a' in (1) is small the following equations for steady state uniaxial deformation are given in the 1, 2 and 3 directions respectively as:

$$\begin{aligned} \sigma^c_{11} &= k_{11} + k_{11}(\eta\,\zeta\,\dot{\lambda})^{1/n} \\ \sigma^c_{22} &= k_{22} + k_{22}(\eta\,\zeta\,\dot{\lambda})^{1/n} \\ \sigma^c_{33} &= k_{33} + k_{33}(\eta\,\zeta\,\dot{\lambda})^{1/n} \end{aligned} \tag{A.15}$$

where $\zeta$ is given in (A.13) and $k_{ii}$ (no sum) are yield parameters. An interesting feature of the flow rule (A.14) is that the ratios of stress in (A.15) remain constant at given rates i.e.

$$\sigma^c_{11}/k_{11} = \sigma^c_{22}/k_{22} = \sigma^c_{33}/k_{33} \tag{A.16}$$

This effect seems reasonable since the stiffness dependence on orientation is mainly due to the relative amount of struts at a given orientation. For example there are more struts oriented in the foam rise direction (Huber and Gibson, 1988) such that it is the stiffer direction.

---

[4] As stated in Section 3.1, the yield parameters $k_{ii}$ (no sum) can be considered the uniaxial compressive yield stresses in the ii direction since 'a' is typically small in (1) for low density foams.